nature nanotechnology

ARTICLES

PUBLISHED ONLINE: 8 FEBRUARY 2016 | DOI: 10.1038/NNANO.2015.336

Plasmonic nanofocused four-wave mixing for femtosecond near-field imaging

Vasily Kravtsov[1], Ronald Ulbricht[1], Joanna M. Atkin[1,2] and Markus B. Raschke[1]*

Femtosecond nonlinear optical imaging with nanoscale spatial resolution would provide access to coupled degrees of freedom and ultrafast response functions on the characteristic length scales of electronic and vibrational excitations. Although near-field microscopy provides the desired spatial resolution, the design of a broadband high-contrast nanoprobe for ultrafast temporal resolution is challenging due to the inherently weak nonlinear optical signals generated in subwavelength volumes. Here, we demonstrate broadband four-wave mixing with enhanced nonlinear frequency conversion efficiency at the apex of a nanometre conical tip. Far-field light is coupled through a grating at the shaft of the tip, generating plasmons that propagate to the apex while undergoing asymptotic compression and amplification, resulting in a nonlinear conversion efficiency of up to 1×10^{-5}. We apply this nonlinear nanoprobe to image the few-femtosecond coherent dynamics of plasmonic hotspots on a nanostructured gold surface with spatial resolution of a few tens of nanometres. The approach can be generalized towards spatiotemporal imaging and control of coherent dynamics on the nanoscale, including the extension to multidimensional spectroscopy and imaging.

Controlling light with light requires large and broadband optical nonlinearities. One promising route is to use deep subwavelength confinement of optical fields enabled by surface plasmon modes. The resulting mode confinement leads to enhancement of the light–matter interaction and nonlinear optical effects[1].

A high degree of localization of optical energy has traditionally been provided through localized surface plasmon resonances. However, the achievable bandwidth is limited due to the finite plasmon lifetime. Ohmic losses cause rapid heating of the entire plasmonic structure, with potential damage at high optical fields. Furthermore, the direct excitation of localized plasmons with far-field radiation creates scattered background fields that undermine contrast and sensitivity in spectroscopic applications[2,3]. In contrast, by using nanofocusing of surface plasmon polaritons (SPPs)[4,5], the excitation can be non-local. Adiabatic compression upon propagation on a tapered metal structure provides broadband and background-free subwavelength confinement of the optical field[6–9]. This enables efficient nonlinear excitation of near-field coupled emitters, as demonstrated in multiphoton luminescence of Er^{3+} ions[10] or extreme-ultraviolet emission of Xe atoms[11,12]. Nanofocused SPPs asymptotically slow down during propagation with a decrease in group velocity[5,13] and the associated mode volume compression in the propagation direction, which contributes to the total three-dimensional confinement and enhanced nonlinear conversion efficiency.

Third-order nonlinear effects are particularly relevant for ultrafast spectroscopy for several reasons. They are less constrained by symmetry than second-order effects[14], enable all-optical control through modification of the refractive index by light[15] and allow probing of quantum coherence and coupling of excitations in multidimensional spectroscopies, as well as vibrational dynamics with coherent anti-Stokes Raman spectroscopy[16].

The use of plasmonic confinement can bring the footprint of optical devices and the spatial resolution of spectroscopic techniques to the nanometre scale. Previously, plasmon-enhanced third-order nonlinearities have been investigated in systems supporting localized surface plasmon resonances, through third-harmonic generation[17] and non-degenerate four-wave mixing (FWM)[18–22]. Self-phase modulation[23] and self-focusing[24] have been discussed for uncompressed SPPs, as well as FWM of SPPs with far-field radiation[25,26]. However, signal levels for reaching higher-order nonlinearities have been limited by excitation power requirements approaching the damage threshold of the nanostructures.

In this article, we demonstrate ultrafast and broadband FWM in plasmonic nanofocusing with a high nonlinear conversion efficiency of up to 1×10^{-5}. The nonlinear signal is highly localized in a nanoscopic volume at the tip apex and provides for the implementation of new nanospectroscopies, in particular when combined with full control of the optical waveform of the nanofocused light. As an example application, we use nanofocused FWM to image the nanoscale spatial inhomogeneities of the few-femtosecond coherent dynamics of localized surface plasmon hotspots at the edge of a Au film.

FWM on a metal tip

In the present experiment (see Methods), the third-order nonlinear optical signal is generated on a three-dimensional conical gold tip through adiabatic nanofocusing of grating-coupled ultrafast SPPs (Fig. 1a). SPPs propagate towards the apex of the tip and experience asymptotic mode volume compression with associated field enhancement, which leads to increasingly efficient generation and far-field emission of the nonlinear optical response at the tip apex.

We first characterize the nonlinear signal from the apex of a free-standing tip that is not interacting with the sample. To observe the FWM response, we spectrally limit the excitation light with a 785 nm long-pass filter (optical density of >6) and detect the generated FWM signal at shorter wavelengths through a 760 nm short-pass filter. Figure 1b presents normalized spectra of the apex emission, with a tip-generated nonlinear FWM signal ($\lambda < 760$ nm) and fundamental SPP light scattered at $\lambda > 785$ nm.

The power dependence of the spectrally integrated FWM signal is shown on a log–log scale in Fig. 1c (circles). The linear fit (red line) with a slope of 3.01 ± 0.08 confirms the expected cubic dependence in the fundamental laser power.

The generation process of blueshifted FWM by mixing of three spectral components within the broadband pulse[27,28] is illustrated

[1]Department of Physics, Department of Chemistry, and JILA, University of Colorado, Boulder, Colorado 80309, USA. [2]Department of Chemistry, University of North Carolina, Chapel Hill, North Carolina 27599, USA. *e-mail: markus.raschke@colorado.edu

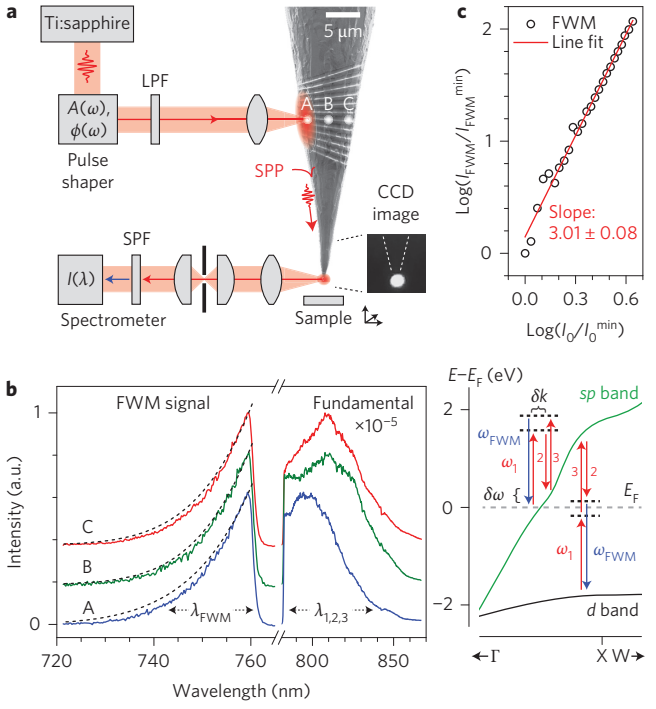

Figure 1 | FWM of nanofocused surface plasmon polaritons. a, Schematic of the experiment: ~10 fs pulses from a Ti:sapphire laser are shaped in spectral amplitude $A(\omega)$ and phase $\phi(\omega)$, spectrally limited by a long-pass filter (LPF), and focused onto the Au tip (not to scale). SPPs are launched through grating-coupling under varying conditions A–C and nanofocused at the apex. Apex emission (inset: charge-coupled device (CCD) camera image, tip shape indicated by dashed lines) is detected with a spectrometer through a short-pass filter (SPF). **b**, Left: FWM ($\lambda < 760$ nm) and fundamental SPP ($\lambda > 785$ nm, attenuated by 10^5) spectra for varying coupling conditions A–C. Right: illustration of possible mechanisms of FWM for the generation of blueshifted ω_{FWM} emission within the band diagram of Au (where E_F indicates Fermi energy). The FWM process can involve resonant contributions: an intraband excitation within the *sp* band of Au (left), with required momentum δk provided by the plasmonic near-field and a two-photon interband transition from the *d* band to the *sp* band (right). **c**, Power dependence of spectrally integrated FWM signal on a log–log scale (circles), with a cubic fit (red line) showing slope of 3.01 ± 0.08.

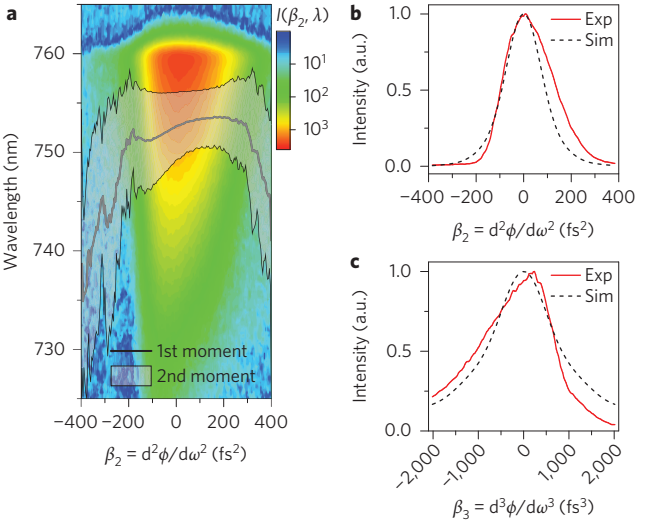

Figure 2 | FWM dependence on spectral phase of the excitation pulse. **a**, FWM spectrum as a function of group velocity dispersion β_2 applied to the laser pulses, with first (black curve) and second (grey area) moments of the spectral distribution. **b**, Spectrally integrated FWM intensity as a function of β_2 (red solid line), together with simulation results (black dashed line). **c**, FWM intensity as a function of the third-order dispersion β_3 (red solid line) and simulation result (black dashed line).

in the right panel of Fig. 1b, with possible pathways[29] as indicated within the band diagram of Au. Both the intraband excitation ($\delta\omega < 0.2$ eV) of the conduction electrons within the dispersive *sp* band of Au near the Fermi level (left) and the two-photon interband transition (~3.1 eV) from the *d* band to the *sp* band (right) can contribute to the FWM process. In contrast to far-field FWM, the intraband contribution could be enhanced with the required momentum $\delta k \approx 1 \times 10^6$ cm^{-1} provided by the momentum distribution of the near-field of the strongly confined plasmon oscillation at the tip apex corresponding to a radius $r_{tip} < \pi/\delta k \approx 50$ nm. The contribution of the *d*-band electrons to the nonlinearity of noble metals has been discussed previously[30] and is supported by the observed slow decoherence of holes at the top of the *d* band[31].

The observed nonlinear signal of the free-standing tip can in principle include contributions from nonlinear processes other than FWM, for example, two-photon photoluminescence of Au[20] or self-phase modulation-induced broadening of the SPP spectrum[23]. However, the results, in particular the clear cubic power dependence in Fig. 1c, show that those effects are at least two orders of magnitude smaller and thus negligible in our case.

We can control the spectral shape of the apex field within the available pump bandwidth by varying the coupling conditions by shifting the incident beam laterally relative to the grating (Fig. 1a, beam positions are indicated by A, B and C). The highest FWM intensity is observed when coupling in a larger bandwidth at position B, while the effect on the FWM spectral shape is minimal as seen for the normalized FWM spectra in Fig. 1b. The spectral intensity $I_{FWM}(\omega)$ of the generated FWM signal is expected to follow from the fundamental SPP spectrum $\tilde{E}(\omega)$, with all possible frequencies $\omega_{1,2,3}$ within its bandwidth:

$$I_{FWM}(\omega) \propto \left| \iiint_{-\infty}^{\infty} d\omega_{i=1,2,3} \chi^{(3)}(-\omega; \omega_1, -\omega_2, \omega_3) \tilde{E}(\omega_1)\tilde{E}^*(\omega_2)\tilde{E}(\omega_3)\delta(\omega - \omega_1 + \omega_2 - \omega_3) \right|^2 \quad (1)$$

The simulated FWM spectra (Fig. 1b, black dashed lines), modelled based on the assumption of transform-limited pulses at the apex $\tilde{E}(\omega) = \sqrt{I_{SPP}(\omega)}$, show good agreement with the experimental data, except for small deviations that are probably due to the low but finite dispersion introduced in the nanofocusing process[32].

The FWM response, as defined by equation (1), strongly depends on the spectral phase of the nanofocused SPP field. We investigate this dependence experimentally by introducing group velocity dispersion β_2 and third-order dispersion β_3 to the spectral phase $\phi(\omega) = (\beta_2/2)(\omega - \omega_0)^2 + (\beta_3/6)(\omega - \omega_0)^3$ of the laser pulses with central frequency ω_0 using the pulse shaper. Figure 2a shows the evolution of the measured FWM spectra as a function of applied group velocity dispersion (note the logarithmic intensity scale). Transformation of the spectral shape is indicated by the first moment $m_1 = \int \lambda I(\lambda) d\lambda / \int I(\lambda) d\lambda$ (black curve) and normalized second moment $m_2 = \int (\lambda - m_1)^2 I(\lambda) d\lambda / \int I(\lambda) d\lambda$ (grey area) of the spectral distribution. The asymmetry in the detected FWM spectrum is responsible for the observed shift between the first moment and the intensity peak position. When the group velocity dispersion approaches zero, the FWM response grows in intensity and acquires a steeper spectral shape. The measured dependencies of the spectrally integrated FWM signal on β_2 and β_3 are shown in Fig. 2b,c (red solid lines), respectively. Although they are in good qualitative agreement with the simulation (black dashed lines), systematic deviations are observed, such as a slight asymmetry with

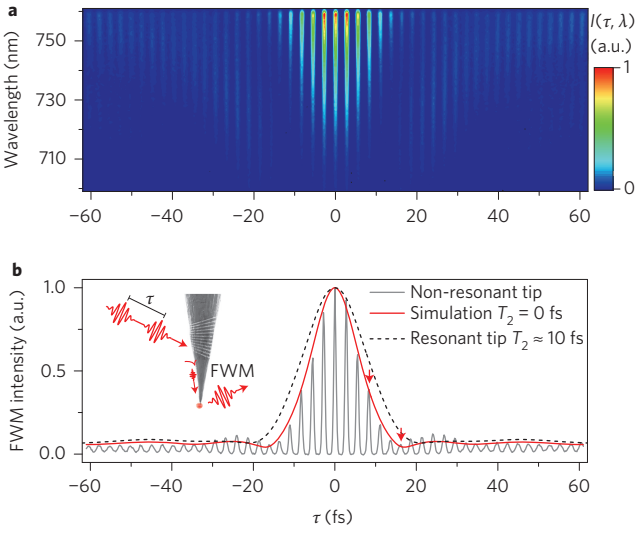

Figure 3 | Dynamics of tip-generated FWM. a, Interferometric FWM spectrogram for two-pulse excitation with inter-pulse delay τ. **b**, Spectrally integrated FWM autocorrelation traces: experimental results for the case of non-resonant tip (grey) and simulation assuming a tip response with dephasing time of $T_2 = 0$ fs (red solid line, envelope only). The broader trace is for a resonant tip, due to excitation of a localized surface plasmon at the apex with dephasing time $T_2 \approx 10$ fs (black dashed line, envelope only). Red arrows indicate delay values selected for the ultrafast nano-imaging measurement. Inset: Schematic of the experiment with two pulses coupled into the tip and the FWM from the apex detected as a function of the inter-pulse delay τ.

respect to positive or negative β_2 and β_3, as well as a finite value of $\beta_3 \approx 200$ fs^3 at the maximum of $I_{FWM}(\beta_3)$. These deviations point towards an additional spectral phase distortion $\delta\varphi_{SPP}(\omega)$ of the SPP that is introduced during its propagation on the tip.

To verify the coherent nature of the FWM signal and estimate the timescale of the tip third-order nonlinear response $\chi^{(3)}$, we performed two-pulse correlation measurements. To this end, collinear pulse pairs with variable time delay τ and zero phase offset $\delta\phi = 0$ were generated by the pulse shaper and coupled into the tip. Figure 3 shows the FWM signal as a function of τ, with full spectrogram $I(\tau, \lambda)$ in Fig. 3a, and spectrally integrated autocorrelation trace (grey) in Fig. 3b. To simulate the two-pulse correlation, we assume a resonant response, characterized by dephasing time T_2 and centre frequency ω_0 as $\chi^{(3)}(-\omega; \omega_1, -\omega_2, \omega_3) \propto [D(\omega)\,D(\omega_1)D(-\omega_2)\,D(\omega_3)]^{-1}$, where $D(\omega_j) = \omega_0^2 - \omega_j^2 - 2i\omega_j/T_2$ and $\omega = \omega_1 - \omega_2 + \omega_3$. The results of the simulation, using the experimental SPP input spectrum and an instantaneous response of the tip with $T_2 = 0$ fs (Fig. 3b, red, only the envelope is shown for clarity), describe the experimental data well, including the long tail due to the sharp cutoff edge of the long-pass filter. The near-instantaneous FWM response from this tip is characteristic for most tips in our experiment. The non-resonant character of the tip response makes it a suitable probe for ultrafast spectroscopy with few-femtosecond time resolution and can provide an all-optical analogue for novel electron-based multidimensional spectroscopies[33]. In contrast, some tips exhibit a localized surface plasmon resonance at the apex within the pulse spectral range, as discussed previously[34]. This gives rise to a wider autocorrelation trace (Fig. 3b, resonant tip, black dashed line, envelope only) described by a resonant excitation with dephasing time $T_2 \approx 10$ fs (Supplementary Fig. 2). This value is within the range of typical dephasing times of localized plasmons[35].

Coherent ultrafast nanoimaging

As a third-order nonlinear response, FWM is highly sensitive to the local electric field enhancement at the tip apex. Resonant near-field interaction with a sample at close proximity will thus modify the FWM transient response. We used this effect to investigate the spatial inhomogeneity of the plasmon dynamics at a rough step edge of a 100-nm-thick Au film evaporated on a Si substrate. We scanned the tip at a constant tip–sample gap of ~5 nm (see Methods) and detected the spatial variation of the near-field coupled optical FWM response. Figure 4 shows the spectrally integrated FWM (Fig. 4a) and atomic force microscopy (AFM) topography (Fig. 4b), acquired simultaneously. The high sensitivity of the FWM signal to the local optical field results in high contrast (see Supplementary Fig. 3 for a comparison with linear imaging) and reveals the localized plasmon-enhanced response of two major and one minor 'hotspots'[36] indicated in Fig. 4a as S_1, S_2 and S_3. Figure 4e shows a line trace across S_3 and S_1 (white dashed line in Fig. 4a,b), with a spatial resolution sufficient to observe S_3 with ~50 nm spatial extent.

We then investigated the femtosecond dynamics of these localized plasmonic modes using two-pulse excitation in consecutive FWM imaging for variable inter-pulse delays τ of 0, 8.2 and 16.4 fs, corresponding to the constructive interference peaks in the autocorrelation trace as shown in Fig. 3b (red arrows). Figure 4c shows the temporal evolution of the FWM response. With the colour scale normalized to the FWM intensity at spot S_1, this already qualitatively reveals different coherent dynamics of S_2 and S_3 when compared to S_1. The FWM intensity of S_2 is initially larger than S_1 (top, $\tau = 0$ fs), but decays faster than S_1 (bottom, $\tau = 16.4$ fs). Similarly, faster dynamics is observed at S_3. To quantify the differences in dephasing, the FWM intensities at S_1 and S_2 were averaged over the dashed circular regions as shown in Fig. 4a, normalized to their values at $\tau = 0$ fs and plotted in Fig. 4d as black and red symbols, respectively. Corresponding two-pulse correlation analysis (Supplementary Fig. 4) shows similar resonant wavelengths for S_1 and S_2 of $\lambda_0 = 800 \pm 20$ nm and $\lambda_0 = 790 \pm 20$ nm, yet different dephasing times of $T_2 = 16 \pm 3$ fs and $T_2 = 10 \pm 2$ fs, respectively (Fig. 4d, black and red lines).

Additionally, the signal from the Au film exhibits a finite dephasing time itself, with faster dephasing in the vicinity of the localized plasmonic modes, as is evident from the destructive interference feature along the film edge in Fig. 4c. A possible interpretation of the observed faster dephasing is the Fano-type interference between the localized excitation and delocalized plasmonic modes near S_1, S_2 and S_3.

We note that the FWM signal is generated in the tip as well as in the near-field coupled sample volume in the vicinity of the tip apex. In general, tip plasmon dynamics needs to be taken into account in the analysis of the measured time-resolved signals. However, due to the near-instantaneous response of the tip in our experiment, we expect the coherent dynamics of the plasmonic hotspots to remain unaffected.

Prospects of coherent nonlinear nanospectroscopy

To use plasmonic nanofocusing for spatiotemporal scanning probe imaging, the generated FWM signal has to be localized in a nanoscopic volume. In contrast to earlier work on grating-coupled second-harmonic generation[7,32], where the nonlinear response is intrinsically localized at the apex because of the broken symmetry in the axial direction, the FWM signal is continuously generated upon SPP propagation. Due to the near-degenerate character of the observed FWM process and low wavelength dispersion of the SPPs, the radius-dependent coherence length is given by $l_c(r) \approx \pi c/(2n_1(r)\omega_1 - n_2(r)\omega_2 - n_{FWM}(r)\omega_{FWM})$ (calculation in Fig. 5a, red dashed line), where $\omega_1 = 1.59$ eV and $\omega_2 = 1.45$ eV approximately define the frequency range of the fundamental SPP spectrum and $n(r)$ is the radius-dependent effective index of refraction. The coherence length is an order of magnitude larger than the SPP propagation length $l_d(r) = 1/(2\mathrm{Im}(k_{SPP}(r)))$ (red dash-dotted line) for all radii r. The FWM process is therefore almost perfectly phase-matched[27,28].

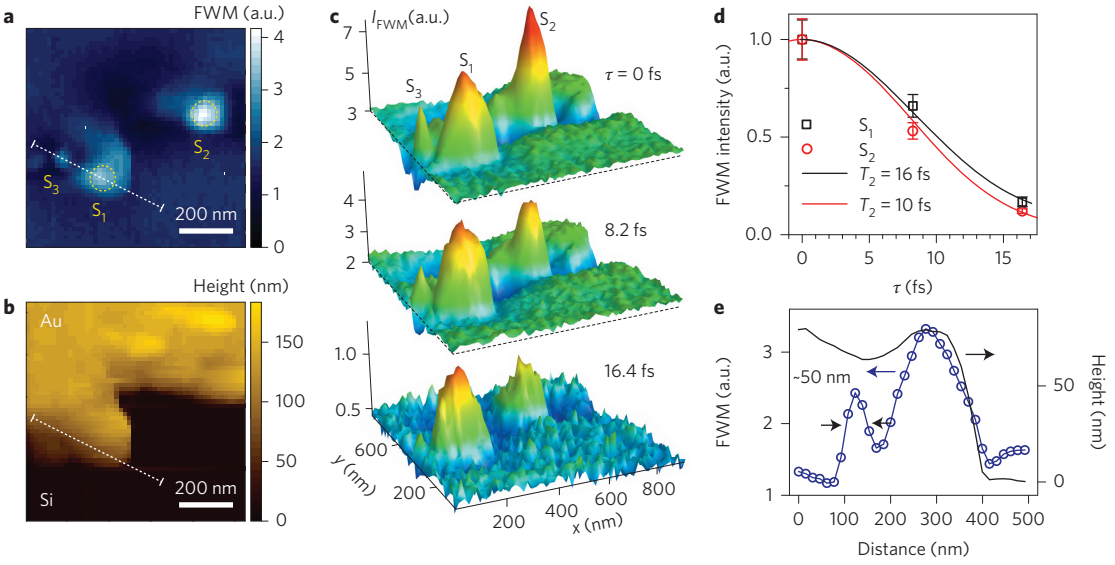

Figure 4 | Femtosecond FWM nanoimaging of coherent plasmon dynamics in gold. a, Near-field FWM image of a Si–Au step, showing 'hotspots' S_1, S_2 and S_3. **b**, Simultaneously acquired AFM topography. **c**, FWM images of the same region with two-pulse excitation, corresponding to an inter-pulse delay of $\tau = 0$ fs (top), 8.2 fs (middle) and 16.4 fs (bottom), demonstrating evolution of the relative intensities in spots S_1, S_2 and S_3. **d**, FWM intensity in S_1 and S_2 for the three delays, showing variation in dephasing time T_2, with simulation for $T_2 = 16$ fs (black solid line) and $T_2 = 10$ fs (red solid line). **e**, Line profiles of FWM signal (blue), showing ~50 nm spatial resolution, and AFM topography (black), extracted from **a** and **b** along the white dashed lines.

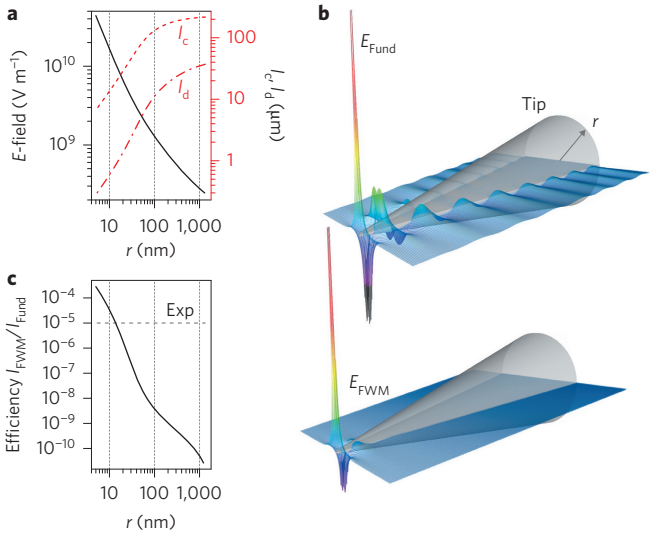

Figure 5 | Localization of FWM response in adiabatic nanofocusing. **a**, Magnitude of the optical electric field of the nanofocusing SPP (black, left axis), FWM coherence length l_c (red dashed line, right axis) and propagation length l_d (red dash-dotted line, right axis) as functions of tip radius r. **b**, Evolution of fundamental (E_{Fund}, top) and FWM (E_{FWM}, bottom) electric field magnitudes along the tip, calculated in the adiabatic approximation. **c**, Ratio of FWM and fundamental emission intensities from the tip apex, which represents the FWM generation efficiency, as a function of apex radius r, calculated for a tip with half-angle 8° and SPP propagation distance 15 m. Grey dashed line indicates the maximum efficiency observed in the experiment.

However, due to the rapid increase of the SPP field at the tip apex, as predicted by the adiabatic model of nanofocusing (Fig. 5a, black), most of the FWM signal is expected to originate primarily from the near-apex region. This is illustrated in Fig. 5b, which shows the calculated field distribution for both fundamental and FWM fields. It highlights the dramatic signal increase due to the adiabatic compression of the fundamental field, further amplifying the already nonlinear dependence of the FWM process.

To quantify the localization of the FWM response, we calculated the FWM field at the tip apex as a function of the apex radius using the adiabatic model[5] (Supplementary Fig. 5). We estimate the initial E-field of the SPP as $\sim 2 \times 10^8$ V m^{-1}, based on the experimental conditions, and use an estimate for the Au nonlinear susceptibility of $\chi^{(3)} \approx 1 \times 10^{-19}$ m^2 V^{-2} (ref. 37).

The result of the calculation for the FWM efficiency defined as a ratio of the FWM and fundamental apex emission $\eta = I_{FWM}/I_{Fund}$ is shown in Fig. 5c, and is seen to increase rapidly for apex radii $\lesssim$50 nm. Based on this model, the maximum values of $\eta \approx 1 \times 10^{-5}$ observed in our experiments would correspond to a tip radius of $r \approx 15$ nm. Typical efficiency values for the range of tips investigated are $\eta \approx 1 \times 10^{-7}$ to 1×10^{-6}, corresponding to $r \approx$ 20–50 nm, that is, in good agreement with apex radii as determined by scanning electron microscopy and the $\lesssim$50 nm spatial resolution observed in Fig. 4a,e in FWM imaging.

Nanofocused FWM provides a tool for nanoimaging of ultrafast coherent dynamics, as demonstrated in Fig. 4. Our dephasing times of localized plasmon modes on the rough Au edge of 10–16 fs are in agreement with the range of typical values controlled by structural heterogeneity and radiative decay[34,35,38]. This, together with the shorter dephasing times of 5–6 fs measured on a similar rough metal edge of Ag using time-resolved photoelectron emission microscopy (PEEM)[36], confirms that tip–sample coupling only weakly perturbs the plasmon dynamics measured. The longer dephasing times measured in our case could be due to a possible interference with delocalized plasmon modes. We note that our values are considerably shorter than femtosecond PEEM results from rough Ag films[39]. There, based on ~50 fs pulsed excitation, dephasing times of ~100 fs were reported. However, these results are possibly related to a superposition of propagating modes[40] rather than strongly localized plasmons.

Ultrafast nanofocused nanoimaging complements related efforts for spatiotemporal imaging, building on early attempts to combine femtosecond optical spectroscopy with scanning probe microscopy[41]. Based on the reduced background and enhanced optical nonlinearity, adiabatic nanofocusing exceeds the performance of both conventional aperture-based and apertureless ultrafast near-field

optical microscopy[42,43]. Compared with ultrafast PEEM[36,39] or transmission electron microscopy (TEM)[44], albeit at the expense of field of view and imaging speed, our approach is experimentally more simple and does not require ultrahigh-vacuum conditions, which provides for a broad application space. As an all-optical technique, in contrast to ultrafast scanning tunnelling microscopy[45–47], it can image both linear and nonlinear coherent dynamic processes. The $\lesssim$50 nm resolution demonstrated (Fig. 4e) is already comparable to femtosecond PEEM experiments, but even higher spatial resolution has been observed with plasmonic nanofocusing[48], and extension to single nanometres or even below should be possible with improved tip designs.

Conclusions

We have investigated intrapulse FWM nanofocused on a Au tip for ultrafast nanoimaging of few-femtosecond coherent plasmon dynamics. Due to the asymptotic compression of the SPPs associated with the nanofocusing process, the nonlinear signal is highly localized in a nanoscopic volume at the tip apex. The nonlinear conversion efficiency is greatly enhanced, which provides for a highly sensitive nanoprobe for ultrafast near-field microscopy and spectroscopy.

Our FWM femtosecond time-resolved nonlinear nanoimaging can lead to coherent, ultrafast and multidimensional all-optical near-field spectroscopic imaging. The FWM response of the tip itself, sensitive to the spectral phase of the nanofocused broadband pulse, provides a reference signal for the pulse optimization and, together with deterministic pulse shaping, full control of the waveform in the nanoscopic probe volume. This enables the use of phase-cycling[49] and quasi-phase-cycling[50] methods to suppress unwanted background signal and select particular excitation pathways, whereas the use of conventional phase-matching based implementations is limited due to the broad distribution of wave vectors associated with the nanofocused light.

Methods

Methods and any associated references are available in the online version of the paper.

Received 18 August 2015; accepted 16 December 2015; published online 8 February 2016

References

1. Kauranen, M. & Zayats, A. V. Nonlinear plasmonics. *Nature Photon.* **6,** 737–748 (2012).
2. Berweger, S., Atkin, J. M., Olmon, R. L. & Raschke, M. B. Adiabatic tip–plasmon focusing for nano-Raman spectroscopy. *J. Phys. Chem. Lett.* **1,** 3427–3432 (2010).
3. Sadiq, D. *et al.* Adiabatic nanofocusing scattering-type optical nanoscopy of individual gold nanoparticles. *Nano Lett.* **11,** 1609–1613 (2011).
4. Babadjanyan, A. J., Margaryan, N. L. & Nerkararyan, K. V. Superfocusing of surface polaritons in the conical structure. *J. Appl. Phys.* **87,** 3785–3788 (2000).
5. Stockman, M. I. Nanofocusing of optical energy in tapered plasmonic waveguides. *Phys. Rev. Lett.* **93,** 137404 (2004).
6. De Angelis, F. *et al.* Nanoscale chemical mapping using three-dimensional adiabatic compression of surface plasmon polaritons. *Nature Nanotech.* **5,** 67–72 (2010).
7. Schmidt, S. *et al.* Adiabatic nanofocusing on ultrasmooth single-crystalline gold tapers creates a 10-nm-sized light source with few-cycle time resolution. *ACS Nano* **6,** 6040–6048 (2012).
8. Choo, H. *et al.* Nanofocusing in a metal–insulator–metal gap plasmon waveguide with a three-dimensional linear taper. *Nature Photon.* **6,** 837–843 (2012).
9. Gramotnev, D. K. & Bozhevolnyi, S. I. Nanofocusing of electromagnetic radiation. *Nature Photon.* **8,** 14–23 (2014).
10. Verhagen, E., Kuipers, L. & Polman, A. Enhanced nonlinear optical effects with a tapered plasmonic waveguide. *Nano Lett.* **7,** 334–337 (2007).
11. Park, I. Y. *et al.* Plasmonic generation of ultrashort extreme-ultraviolet light pulses. *Nature Photon.* **5,** 678–682 (2011).
12. Sivis, M., Duwe, M., Abel, B. & Ropers, C. Extreme-ultraviolet light generation in plasmonic nanostructures. *Nature Phys.* **9,** 304–309 (2013).
13. Kravtsov, V., Atkin, J. M. & Raschke, M. B. Group delay and dispersion in adiabatic plasmonic nanofocusing. *Opt. Lett.* **38,** 1322–1324 (2013).
14. Boyd, R. W. *Nonlinear Optics* 3rd edn (Academic, 2008).
15. MacDonald, K. F., Samson, Z. L., Stockman, M. I. & Zheludev, N. I. Ultrafast active plasmonics. *Nature Photon.* **3,** 55–58 (2009).
16. Yampolsky, S. *et al.* Seeing a single molecule vibrate through time-resolved coherent anti-Stokes Raman scattering. *Nature Photon.* **8,** 650–656 (2014).
17. Lippitz, M., van Dijk, M. A. & Orrit, M. Third-harmonic generation from single gold nanoparticles. *Nano Lett.* **5,** 799–802 (2005).
18. Danckwerts, M. & Novotny, L. Optical frequency mixing at coupled gold nanoparticles. *Phys. Rev. Lett.* **98,** 026104 (2007).
19. Kim, H., Taggart, D. K., Xiang, C., Penner, R. M. & Potma, E. O. Spatial control of coherent anti-Stokes emission with height-modulated gold zig-zag nanowires. *Nano Lett.* **8,** 2373–2377 (2008).
20. Palomba, S. & Novotny, L. Near-field imaging with a localized nonlinear light source. *Nano Lett.* **9,** 3801–3804 (2009).
21. Jung, Y., Chen, H., Tong, L. & Cheng, J.-X. Imaging gold nanorods by plasmon-resonance-enhanced four wave mixing. *J. Phys. Chem. C* **113,** 2657–2663 (2009).
22. Genevet, P. *et al.* Large enhancement of nonlinear optical phenomena by plasmonic nanocavity gratings. *Nano Lett.* **10,** 4880–4883 (2010).
23. De Leon, I., Sipe, J. E. & Boyd, R. W. Self-phase-modulation of surface plasmon polaritons. *Phys. Rev. A* **89,** 013855 (2014).
24. Davoyan, A. R., Shadrivov, I. V., Zharov, A. A., Gramotnev, D. K. & Kivshar, Y. S. Nonlinear nanofocusing in tapered plasmonic waveguides. *Phys. Rev. Lett.* **105,** 116804 (2010).
25. Palomba, S. & Novotny, L. Nonlinear excitation of surface plasmon polaritons by four-wave mixing. *Phys. Rev. Lett.* **101,** 056802 (2008).
26. Renger, J., Quidant, R., van Hulst, N., Palomba, S. & Novotny, L. Free-space excitation of propagating surface plasmon polaritons by nonlinear four-wave mixing. *Phys. Rev. Lett.* **103,** 266802 (2009).
27. Min, W., Lu, S., Rueckel, M., Holtom, G. R. & Xie, X. S. Near-degenerate four-wave-mixing microscopy. *Nano Lett.* **9,** 2423–2426 (2009).
28. Suchowski, H. *et al.* Phase mismatch-free nonlinear propagation in optical zero-index materials. *Science* **342,** 1223–1226 (2013).
29. Wang, Y., Lin, C.-Y., Nikolaenko, A., Raghunathan, V. & Potma, E. O. Four-wave mixing microscopy of nanostructures. *Adv. Opt. Photon.* **3,** 1–52 (2011).
30. Hache, F., Ricard, D., Flytzanis, C. & Kreibig, U. The optical Kerr effect in small metal particles and metal colloids: the case of gold. *Appl. Phys. A* **47,** 347–357 (1988).
31. Petek, H., Nagano, H. & Ogawa, S. Hole decoherence of *d* bands in copper. *Phys. Rev. Lett.* **83,** 1931–1934 (1999).
32. Berweger, S., Atkin, J. M., Xu, X. G., Olmon, R. L. & Raschke, M. B. Femtosecond nanofocusing with full optical waveform control. *Nano Lett.* **11,** 4309–4313 (2011).
33. Cui, X. *et al.* Transient excitons at metal surfaces. *Nature Phys.* **10,** 505–509 (2014).
34. Anderson, A., Deryckx, K. S., Xu, X. J. G., Steinmeyer, G. & Raschke, M. B. Few-femtosecond plasmon dephasing of a single metallic nanostructure from optical response function reconstruction by interferometric frequency resolved optical gating. *Nano Lett.* **10,** 2519–2524 (2010).
35. Sonnichsen, C. *et al.* Drastic reduction of plasmon damping in gold nanorods. *Phys. Rev. Lett.* **88,** 077402 (2002).
36. Kubo, A. *et al.* Femtosecond imaging of surface plasmon dynamics in a nanostructured silver film. *Nano Lett.* **5,** 1123–1127 (2005).
37. Boyd, R. W., Shi, Z. & De Leon, I. The third-order nonlinear optical susceptibility of gold. *Opt. Commun.* **326,** 74–79 (2014).
38. Kravtsov, V., Berweger, S., Atkin, J. M. & Raschke, M. B. Control of plasmon emission and dynamics at the transition from classical to quantum coupling. *Nano Lett.* **14,** 5270–5275 (2014).
39. Aeschlimann, M. *et al.* Coherent two-dimensional nanoscopy. *Science* **333,** 1723–1726 (2011).
40. Wang, L.-M., Zhang, L., Seideman, T. & Petek, H. Dynamics of coupled plasmon polariton wave packets excited at a subwavelength slit in optically thin metal films. *Phys. Rev. B* **86,** 165408 (2012).
41. Feldstein, M. J., Vohringer, P., Wang, W. & Scherer, N. F. Femtosecond optical spectroscopy and scanning probe microscopy. *J. Phys. Chem.* **100,** 4739–4748 (1996).
42. Xu, X. G. & Raschke, M. B. Near-field infrared vibrational dynamics and tip-enhanced decoherence. *Nano Lett.* **13,** 1588–1595 (2013).
43. Wagner, M. *et al.* Ultrafast dynamics of surface plasmons in InAs by time-resolved infrared nanospectroscopy. *Nano Lett.* **14,** 4529–4534 (2014).
44. Feist, A. *et al.* Quantum coherent optical phase modulation in an ultrafast transmission electron microscope. *Nature* **521,** 200–203 (2015).
45. Terada, Y., Yoshida, S., Takeuchi, O. & Shigekawa, H. Real-space imaging of transient carrier dynamics by nanoscale pump–probe microscopy. *Nature Photon.* **4,** 869–874 (2010).
46. Cocker, T. L. *et al.* An ultrafast terahertz scanning tunnelling microscope. *Nature Photon.* **7,** 620–625 (2013).

47. Lee, J., Perdue, S. M., Rodriguez Perez, A. & Apkarian, V. A. Vibronic motion with joint angstrom–femtosecond resolution observed through Fano progressions recorded within one molecule. *ACS Nano* **8,** 54–63 (2014).
48. Neacsu, C. C. *et al.* Near-field localization in plasmonic superfocusing: a nanoemitter on a tip. *Nano Lett.* **10,** 592–596 (2010).
49. Keusters, D., Tan, H.-S. & Warren, W. S. Role of pulse phase and direction in two-dimensional optical spectroscopy. *J. Phys. Chem. A* **103,** 10369–10380 (1999).
50. Bloem, R., Garrett-Roe, S., Strzalka, H., Hamm, P. & Donaldson, P. Enhancing signal detection and completely eliminating scattering using quasi-phase-cycling in 2D IR experiments. *Opt. Express* **18,** 27067–27078 (2010).

Acknowledgements

The authors acknowledge funding from the National Science Foundation (NSF grant CHE 1306398), AFOSR (grant #FA9550-14-1-0376) and a partner proposal by the Environmental Molecular Sciences Laboratory (EMSL), a national scientific user facility from the DOE Office of Biological and Environmental Research at Pacific Northwest National Laboratory (PNNL). PNNL is operated by Battelle for the US DOE under contract DEAC06-76RL01830. R.U. acknowledges support by a Rubicon Grant of the Netherlands Organization for Scientific Research (NWO). The authors thank H. Petek and S. Cundiff for discussions.

Author contributions

M.B.R., R.U. and V.K. conceived the experiment. R.U. and J.M.A. contributed to designing the experiment. V.K. performed the measurements and analysed the data. V.K. and M.B.R. wrote the manuscript with contributions from R.U. and J.M.A. All authors discussed the results and commented on the manuscript. M.B.R. supervised the project.

Additional information

Supplementary information is available in the online version of the paper. Reprints and permissions information is available online at www.nature.com/reprints. Correspondence and requests for materials should be addressed to M.B.R.

Competing financial interests

The authors declare no competing financial interests.

Methods

The third-order nonlinear optical signal was generated on a three-dimensional conical gold tip with a half-apical angle of ~10° through adiabatic nanofocusing of SPPs launched on a grating at a distance of ~15 μm from the apex (Fig. 1a). Details of the tip fabrication based on electrochemical etching and focused ion beam milling can be found elsewhere[48]. Broadband pulses with a centre wavelength of ~800 nm and a pulse duration of ~10 fs from a Ti:sapphire laser oscillator passed through a dual-mask liquid-crystal-based amplitude and phase pulse shaper in 4*f* reflection geometry and were focused onto the tip grating with an achromatic lens. To ensure transform-limited pulses at the coupling grating, the dispersion of the optical components was compensated with a multiphoton intrapulse interference phase scan (MIIPS) algorithm[32] (Supplementary Fig. 1). Nanofocusing of the SPPs resulted in highly localized optical fields at the tip apex, which emitted into the far field as a point dipolar source[48]. Tip apex emission was collected through a microscope objective (Olympus, ×50/0.5) in a 90° geometry out of plane with respect to the tip axis and incident k-vector, spatially filtered to reject grating-scattered light and detected with a CCD spectrometer (Princeton Instruments, SP500i).

The tips were mounted on quartz tuning forks for shear-force-based atomic force microscopy (AFM), with ~5 nm tip–sample distance control. The sample was raster-scanned with subnanometre positioning accuracy using a three-axis piezo stage (Physik Instrumente, P-517) operated by an AFM controller (RHK Technology, R9).

The sample was prepared by depositing a 100-nm-thick layer of Au onto a Si substrate at a rate of 0.5 nm s^{-1} by thermal evaporation at a pressure P of $<1 \times 10^{-6}$ mbar. The Au layer was partially lifted off with tape to create a rough step-like Au edge.